Sensor enabled closed-loop bending control of soft beams

2016 Smart Mater. Struct. 25 045018

(http://iopscience.iop.org/0964-1726/25/4/045018)

IOP Publishing Smart Materials and Structures
Smart Mater. Struct. 25 (2016) 045018 (10pp) doi:10.1088/0964-1726/25/4/045018

Sensor enabled closed-loop bending control of soft beams

Jennifer C Case, Edward L White and Rebecca K Kramer

Department of Mechanical Engineering, Purdue University, West Lafayette, IN 47907, USA

E-mail: rebeccakramer@purdue.edu

Received 20 October 2015, revised 8 February 2016
Accepted for publication 9 February 2016
Published 14 March 2016

Abstract

Control of soft-bodied systems is challenging, as the absence of rigidity typically implies distributed deformations and infinite degrees-of-freedom. In this paper, we demonstrate closed-loop control of three elastomer beams that vary in bending stiffness. The most stiff beam is comprised of a single prismatic structure made from a single elastomer. In the next beam, increased flexibility is introduced via an indentation in the elastomer, forming a joint. The most flexible beam uses a softer elastomer in the joint section, along with an indentation. An antagonistic pair of actuators bend the joint while a pair of liquid–metal-embedded strain sensors provide angle feedback to a control loop. We were able to achieve control of the system with a proportional–integral–derivative control algorithm. The procedure we demonstrate in this work is not dependent on actuator and sensor choice and could be applied to to other hardware systems, as well as more complex multi-joint robotic structures in the future.

S Online supplementary data available from stacks.iop.org/sms/25/045018/mmedia

Keywords: closed-loop control, soft structures, responsive materials

(Some figures may appear in colour only in the online journal)

1. Introduction

Robots manufactured from elastomers possess unique functionalities due to their highly deformable structures. This deformability is the source of both the most compelling advantages and most daunting challenges of these systems. The design process for a soft robot involves developing materials, geometries, and control algorithms simultaneously. That interaction is the fundamental contribution of this present work. We describe the interplay between the mechanical design of a soft structure, the application of soft and responsive material actuators and sensors to that structure, and the integration of control algorithms to the resulting soft assembly. This work is a prototype of the design process that would accompany a full soft robot.

Traditional, rigid robotic structures have two general types of joints: rotational and prismatic. The motions of these joints are clearly defined and make finding the forward and inverse kinematics relatively simple. Soft robots, on the other hand, are generally continuously deformable systems and have the potential to deform in any direction and at any point. This complicates the dynamics of soft systems and makes them challenging to control.

We can look towards vertebrates for a potential solution to this problem. Generally, the human body is considered a soft system compared to rigid robots. However, complex joints which can be approximated as rotary or hinge joints still exist inside of this 'soft' system. This is because humans and other vertebrates have stiff skeletal structures. The skeletons give a supporting structure to vertebrates while still being composed of relatively soft materials (compared to materials used in traditional robotics) that still experience viscoelasticity [1]. While adding rigid or stiff components to soft systems can seem limiting, it has allowed vertebrates to operate on a larger scale than purely soft animals, such as caterpillars, worms, and jellyfish. Skeletal structures have also developed to allow vertebrates to accomplish specific tasks. For example, rats have a hinged rib cage that will compress allowing them to squeeze through small holes [2]. Animals with endoskeletons use harder components (bones) held in place by a softer material (cartilage) and moved by contractile actuators (muscles) to operate and move various joints.

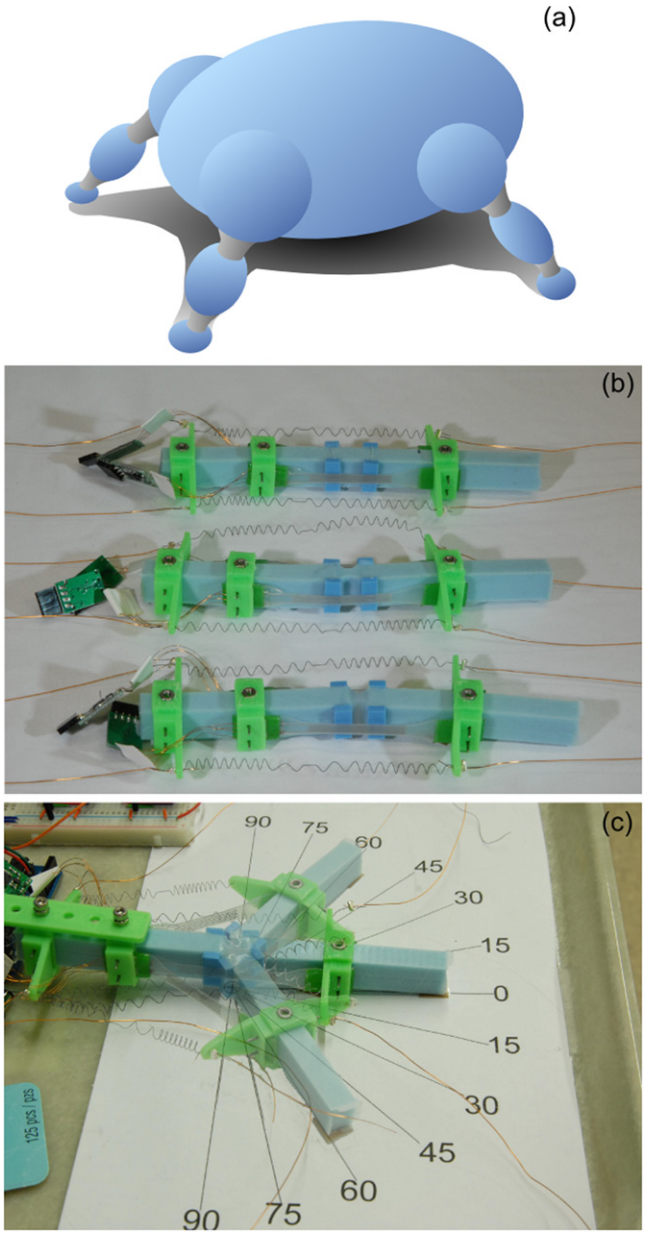

Figure 1. This figure shows (a) a conceptual soft robot based on the deformation localization presented in this work; (b) the three elastomer beams with attached sensors and actuators used in this work; and (c) an image showing a beam in neutral and activated configurations.

Borrowing these concepts, we can utilize geometry and material properties of structures to localize deformation on a soft robotic structure, and therefore make it easier to track the movement of soft structures.

Our goal in this work is to demonstrate three soft structures undergoing localized deformations. Deformation localization serves two purposes. First, it simplifies the kinematic model of the soft structure. Second, it simplifies the proprioceptive feedback problem, since state only needs to be sensed at the soft 'joints,' rather than continuously across the entire structure. We focus on the design fabricated from two dissimilar materials that exhibits motion confined primarily to a soft 'joint' between two harder 'bones.' Multiple joints could be combined with a representative soft body to make a mobile soft robot, as shown conceptually in figure 1(a), or a soft gripper; however, in this work, we confine our study to single joint systems.

In the present work, the three structures were fabricated from Smooth-Sil 935 (Shore hardness: 35A), a relatively stiff silicone elastomer, with the exception of one structure that contains a soft joint fabricated from Dragon Skin 10 Slow (Shore hardness: 10A). This design improves the controllability of the structure while successfully localizing the deformation and maintaining the benefits from using soft polymer materials.

To build a complete closed-loop control system, we integrated elastomer strain gauges to measure joint angle and shape memory alloy (SMA) coils to provide actuation. Using this approach, we are able to directly measure the angle of the joint in the structure and use this information as an input to our control system. A proportional–integral–derivative (PID) control algorithm was used to control the angle of the soft robotic joint. The strain gauges were only sensitive to deformations at the soft joint, although the SMA was connected across a much larger portion of the body (see figure 1 for an overview of the system). Confirmation of the accuracy of the measured angle was obtained by visually observing the robotic joint. We note here that the primary contribution of this work is design for control of soft joints and that our results are independent from specific actuator and sensor choice.

2. Previous work

There is growing interest in control of soft systems with many different approaches [3, 4]. Researchers have experimented with several control strategies to date, including open-loop control [5–8], model-based control [9–11], model-free control [12], and closed-loop control enabled by the inclusion of soft sensors to the robotic system [13, 14]. In this work, we take the latter approach of employing sensors that provide state feedback and enable correction. Given that elastic materials have nonlinear responses at high strains and exhibit viscoelastic behaviors [15, 16], we believe this sensor-enabled approach can be used in conjunction with modeling control approaches to allow for simplified models and to correct for modeling errors.

A further measure to simplify the control problem for soft robots is to localize deformations. The objective of localizing deformation has been achieved by various groups using different means, including film-like shape memory hinges between rigid plates [17, 18], particle jamming [19], hinged shape memory polymer films [20, 21], localized heating of hydrogels [22], gradiated elastomers [23], and localized melting of metal alloys [24]. None of these methods are particularly well-suited to the application we foresee of freestanding elastomer robots, either due to complexity in manufacturing or actuation. Therefore, we elected to passively localize deformation by modifying the structure. These

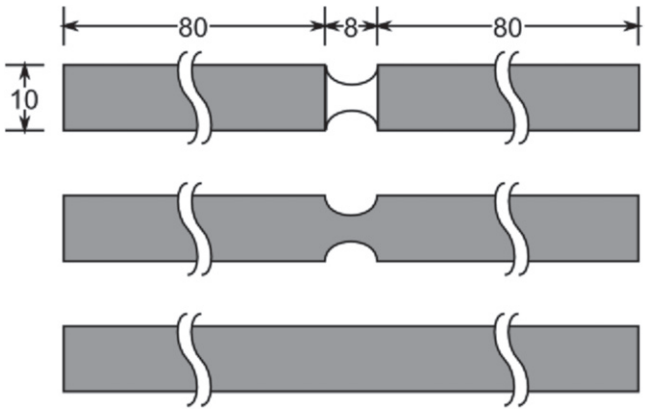

Figure 2. Different elastomer structure designs. From top to bottom: a non-homogenous beam, a non-prismatic beam, and a prismatic beam. The bones of the non-prismatic and non-homogeneous beams are 80 mm × 10 mm × 15 mm with an 8 mm joint connecting the bones together. The prismatic beam has the same overall length as the other two beams. All dimensions are in mm.

modifications, both geometric and material, are easy to apply to any elastomer-based robotic system.

Another design goal is to minimize the mechanical impact of the sensors on the response of the system. Therefore, we wish to minimize the stiffness of the sensors relative to the host structure, which undergoes strains on the order of 100%. In general, soft sensing is a diverse field with many demonstrated approaches of fabrication [25–29]. We take the approach of liquid–metal-embedded elastomer strain gauges because they have very low stiffness and minimal impact on the mechanical properties of the system. Additionally, this type of strain sensor exhibits low noise and consistent response to strain [30]. Room temperature liquid metal alloys made from a combination of gallium and indium are an ideal material to use in this application. Filling microchannels with gallium–indium alloy was first reported by Chiechi, Dickey, and colleagues [31, 32]. Since then, the concept of filling microchannels with liquid metal has been applied to create pressure, force, and touch sensors [33–35], curvature and joint angle sensors [27, 36], and combined strain and pressure sensors [37]. Our strain sensors were very similar to those produced previously, except that we used a different elastomer substrate. Previous groups typically used EcoFlex 00-30 (Smooth-On) as a very soft elastomer. We have found that this material is incompatible with our laser-based approach to fabricating sensors, which we describe below. Instead, we used Dragon Skin 10 Slow (Smooth-On), which was slightly harder, but more compatible with our fabrication process.

We selected SMA as the actuator because it required very little interface hardware compared to pneumatics, which require pumps, valves, pressure sensors, and the like. In SMA systems, the thermally responsive actuators are activated by Joule heating. This results in a very simple interface. Nickel-titanium SMA such as those used in this work were first described by Jackson, *et al* [38]. The thermomechanical response behind the shape memory effect is both complex and well studied [39–46]. This class of materials has been used in a wide range of applications, including robotics, endoscopes, vascular stents, morphing structures, and wearable devices. All of these applications could potentially benefit from the integration of position sensing to achieve finer control during actuation. However, we note here that SMA has several disadvantages as a responsive actuator such as slow deactivation times, thermal sensitivity, and poor energy efficiency, and other soft and responsive actuators such as fluidic actuators, cable driven systems, electroactive polymers, and shape memory polymers could replace the SMA actuators depending on the target application of the system [4].

In this work, we amplified the natural deformation of SMA by introducing a coiled geometry. Nickel–titanium alloys are capable of sustaining strains of $1\% \sim 2\%$ over many cycles. The use of a coiled shape allows us to achieve the required ~60% deformation required overall, while keeping the local deformation in the material small [47]. This requirement was dictated by our target range of motion for the soft system of $\pm 60^{\circ}$ and the location of the attachment points of the SMA actuators. The trade-off is that force output from the actuator is reduced proportionally. Since the elastomer structure used in this work was very deformable, we were able to easily construct actuators capable of providing the required force. The response of the actuator is also a function of the imposed conditions during manufacturing. In this work, we used the results of Seok *et al* to inform our manufacturing approach [48].

As noted previously, SMAs exhibit a complex thermomechanical response. They have a nonlinear response to temperature and large hysteresis effects. Despite this, progress has been made in controlling these materials [49–54]. In the present work, we took the approach of Ikuta *et al* who used tuned PID controllers to overcome the complexities associated with the thermomechanical response. Given the relatively slow actuation and motions required for our work, a properly tuned PID controller resulted in satisfactory control.

In summary, the individual elements used in this work were either inspired by or directly borrowed from previous work. Our focus has been on integrating these elements together in such a way that we can demonstrate closed-loop control of a structure comprised entirely of soft materials. Our long-term goal is to develop the results of this work into more complex soft robotic systems with multiple joints and degrees of freedom that are capable of operating in unstructured environments.

3. Design

3.1. Elastomer beams

The objectives of this system are to localize bending in a specified location along an elastomer beam and to determine if that localized bending facilitates control of the deformation of the elastomer beam. We refer to this specified location as the ‘soft joint’, which will connect ‘soft bones’.

To localize bending, we tested two methods: (1) reducing the width of the joint, and (2) replacing the joint with a softer elastomer. To test the effectiveness of these techniques, we

looked at: (1) a homogeneous elastomer beam with constant width (prismatic beam), (2) a homogeneous elastomer beam with reduced joint width (non-prismatic beam), and (3) an elastomer beam with a softer elastomer at the joint with reduced width (non-homogeneous beam). These configurations are shown in figure 2.

3.2. SMA coils

The transition temperature of the nickel titanium alloy used in this work was approximately 70 °C at no load. However, this transition temperature is a function of the stress of the system. Higher stress causes the transition temperature to increase. Because of this, creating a purely temperature-based control algorithm would not be able to directly control either stress or deformation in the system. Some mechanical feedback is required. Additionally, because we used an antagonistic configuration of SMA, there was an interaction between the two coils that is not present in more traditional actuator systems. As one coil activated, it pulled on and deformed the opposite coil. The force required to complete this was a function of the temperature of the other coil, which itself was changing over time due to free convection. Our approach was to neglect these complexities and treat the system as a black box.

We tested several different combinations of SMA wire diameter and coil diameter before selecting the coil we used in this work. Our goal was to balance the force produced by an active coil with the force required to restore an inactive coil. As expected, tighter coils with larger wire resulted in larger blocking force when active, but also required larger force to return to their neutral length. In the case of a 0.5 mm wire coiled into a 1.6 mm diameter coil, the resulting active force was approximately 7 N with a current of 1.5 A. These forces were sufficient to buckle the soft structure, and was considerably higher than required to meet our objectives. We will point out here that SMA coils could be designed for larger applications by increasing wire diameter and decreasing coil length, although the latter becomes difficult for larger wires.

3.3. Sensor and actuator placement

We placed our sensors and actuators over the joint of the elastomer structure. A sensor and actuator pair was placed on either side of the elastomer structure as seen in figure 3. The sensors must be pre-strained along the length of the elastomer joint so that when the soft structure reaches its maximum angles (in this case, −60° to 60°), neither of the strain sensors buckle. The sensors and actuators are attached to the elastomer structure via mounting brackets, which are pinned in place. The mounting brackets for sensor attachment are pinned 40 mm from the ends of the bones. As shown in figure 3, the SMA coil is attached to one of the sensor mounting brackets. The SMA is also attached to a mounting bracket that is pinned 10 mm from the end of a bone. The mounting locations were selected as a compromise between maximizing the SMA coil length and allowing multiple soft structures to be joined together in a chain.

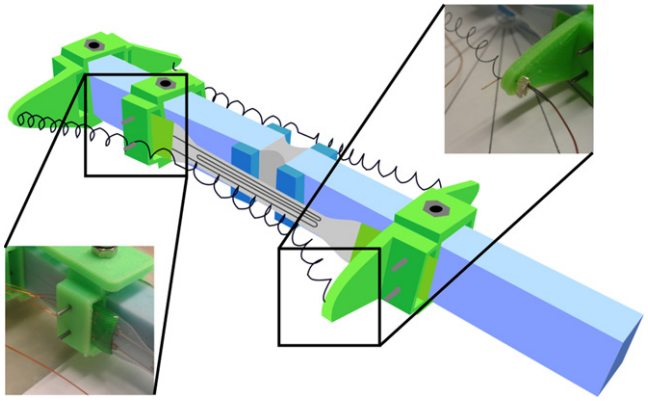

Figure 3. An assembled robotic joint with a non-homogenous beam. The mounting brackets are placed over the beam and locked in place with pins. The elastomer struts are visible on either side of the joint. The pins also lock in the sensors on either side of the beam (seen in the lower left inset) and the SMA is crimped through the holes on the mounting brackets (seen in the upper right inset).

During initial testing, we noticed instabilities in the system due to both the sensors and actuators. The sensors, being pre-strained, would cause the system to snap from one side to the other, which prevented system control over the entire range of motion. To fix this snap-through instability, we added elastomer struts (seen in figure 3) to either side of the joint to discourage this snapping behavior by applying a restoring force on the opposing sensor. Snapping also occurred when the actuators were placed directly next to the elastomer beam. By moving the connection point farther away from the elastomer beam, we were able to eliminate that effect. However, we note that this instability could be leveraged to achieve rapid motion between two regions. For example, this could be used to deploy a structure and lock it in position.

4. Fabrication

A detailed discussion of the fabrication process is provided in the supplemental information. We will only briefly summarize the process here. For the elastomer structure fabrication, three different types of elastomeric beams were fabricated as a part of this study using a combination of stiff elastomer, Smooth-Sil 935, and a softer elastomer, Dragon Skin 10, both from Smooth-On. These elastomers were cast in 3D printed molds, shown in figure 4. For the liquid–metal-embedded elastomer sensor fabrication, we created microchannels in elastomer substrates using a laser. These microchannels were then filled with liquid metal and sealed, completing the sensor. The sensors were fabricated from Dragon Skin 10 elastomer, which is the same soft elastomer used the beam structures. This process is illustrated in figure 5. Additional information on this class of sensors can be found in our previous work [30]. For the actuator fabrication, nickel–titanium wires were programmed into coils at a high temperature.

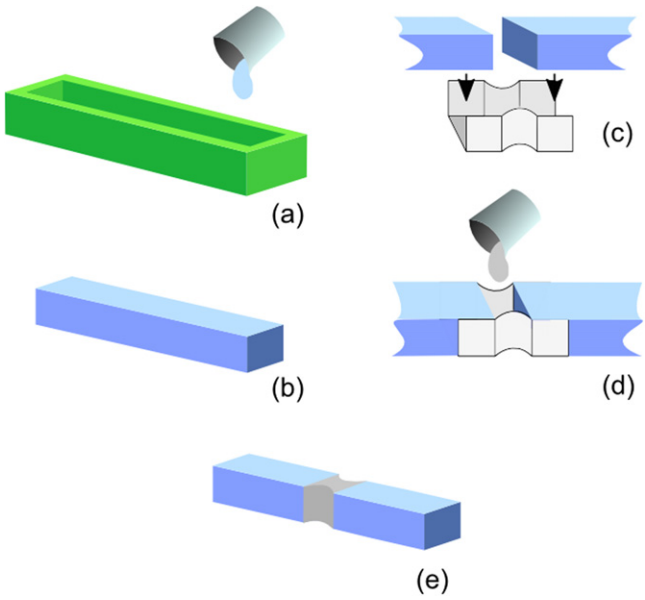

Figure 4. Fabrication process for elastomer beams: (a) Smooth-Sil 935 is poured into a mold and leveled with the flat side of a plastic knife and cured at room temperature overnight (length of molds vary for beam type: 168 mm for a prismatic beam and 80 mm for non-prismatic and non-homogeneous beams); (b) cured beams and bones are removed from the molds (this is the final fabrication step for the prismatic beam); (c) two bones are placed in compression fitted joint mold; (d) either Smooth-Sil 935 or Dragonskin 10 was poured into joint mold and cured overnight in room temperature for the non-prismatic or non-homogeneous beam, respectively; (e) finished joint system removed from the mold (a non-homogeneous beam is shown here).

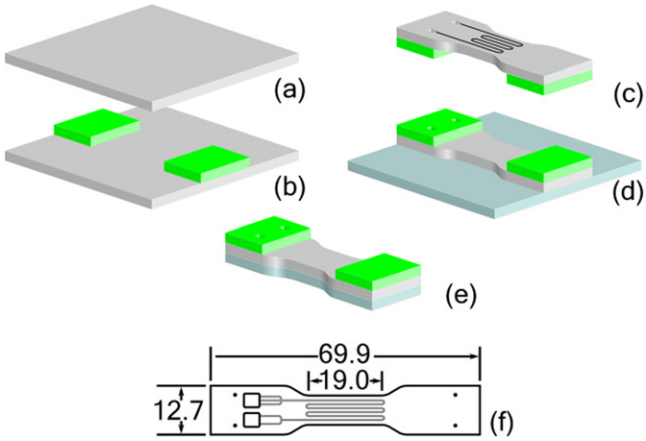

Figure 5. The elastomer sensors are fabricated from two films sandwiching a microchannel pattern. The first film (gray) is created by rod coating liquid elastomer on a polymer substrate (a). Elastomer-infused fabric reinforcement pads (green) are bonded to the upper surface of the film (b). This film is removed from the polymer backing (not shown) and inverted. A laser is used to pattern the microchannels into, and cut the sensor from, the film (c). The resulting half-sensors are then cleaned, inverted so that the channels are facing down, and bonded to a second film of elastomer (d). The complete assembly is then cut from the film to final shape with a laser (e). A schematic of the finished sensor is shown in (f). Dimensions are in millimeters.

The programming procedure was similar to that reported in [55]. In this work, we have used a 'counter-coil' design for our SMA actuators, which eliminates the torque produced by the coils by combining equal-length clockwise and counter-clockwise segments.

5. System integration

We used rigid mounting brackets to attach sensors and actuators to the outside of the soft structure. These brackets were printed from PLA filament using a printrbot simple FDM printer. Two different styles of mounting brackets were used, one with and one without horns to attach SMA. The mounting brackets served two functions. First, they provided a rigid attachment point for the SMA to the soft structure. Second, they held the SMA far enough away from the body to limit the snapping instability observed at large deflections. Given the low forces observed in this structure, the strength of the 3D printed parts was not a factor.

These mounting structures were held in place with pins that passed through the mounting bracket and the soft bones of the structure. This resulted in a very mechanically stable attachment scheme. In the case of the brackets holding the sensors, these pins passed through the fabric reinforcement pads on the sensor body as well, holding them securely to the body. SMA was attached to the mounting brackets by passing the wire through holes in the brackets, then joining the SMA with a copper wire using a metal crimp. The crimp not only ensured electrical contact between the copper lead wire and the SMA, it also provides mechanical attachment since the crimp is larger than the hole in the bracket.

6. Experimental setup

The experimental setup consisted of the soft structure with attached sensors and actuators and the interface electronics. The structure was controlled, and data collected, via an Adruino Uno microcontroller connected to a laptop computer. We designed the soft structure to be modular so that the three different structure configurations could easily be secured with the use of two bolts. Each soft structure had twelve electrical connections: two on each SMA (four total) and four on each sensor (eight total). We were able to remove and replace structures in the fixture within a few minutes.

6.1. Test apparatus

The soft structure was clamped on one end and free to rotate on the other end. We used a printed angular scale attached to the table under the robot to facilitate calibration and monitoring of the robot during operation (see figure 1(c)). We used double-sided tape to affix 1 cm square pieces of PTFE film to the bottom of the 3D printed attachment brackets to reduce friction and facilitate smoother motion.

The two 3D printed attachment brackets on the non-moving side of the structure are bolted to another 3D printed

bracket, which is in turn clamped to a standard laboratory ring stand. This rigidly held the non-moving part of the structure in place.

6.2. Electrical setup

The system uses three power supplies. The Arduino used for communication and control is powered with a 12 V laptop-style power supply. This is not required, but we found that it provided more reliable performance than using power from the USB. The SMAs are powered with an independent Korad KA3005D power supply set at 6.00 V with a maximum output current of 1.00 A. A second Korad KA3005D is used to provide a 2.50 V reference for the sensor signal conditioning electronics.

The angle of the robotic structure was measured using two liquid metal strain sensors attached at the joint. In order to read these two sensors, we used a pair of custom-built signal conditioning circuits. These circuits provide a constant 100 mA current to the sensors while measuring the voltage drop across the resistive sensor element. The resulting voltage difference is then read by a ADS1115 16-bit ADC and communicated to the Arduino Uno. This circuit is shown in figures 6(a) and (b).

The SMA coils are powered by controlled-current supplies. These were built from IRF 510 N-channel MOSFETs controlled by OPA347 operational amplifiers. The amplifiers sensed the voltage drop across a shunt resistor, and drove the MOSFETs such that a desired shunt voltage was achieved. We selected components such that the MOSFETs would nominally be able to supply 700 mA when $V_{GS} = 5$ V. This effectively limited the maximum current that could pass through the SMA actuators. The setpoint voltage was provided via an DAC output from the Arduino Uno. Since the DAC on the Arduino uses a 1 kHz signal to produce approximate analog outputs, we passed that signal through a low-pass filter with a cutoff frequency of 30 Hz before sending it to the current control amplifier. This reduced electrical noise in the system since the MOSFET operated as an analog device, instead of in a PWM mode. This circuit is shown in figure 6(c).

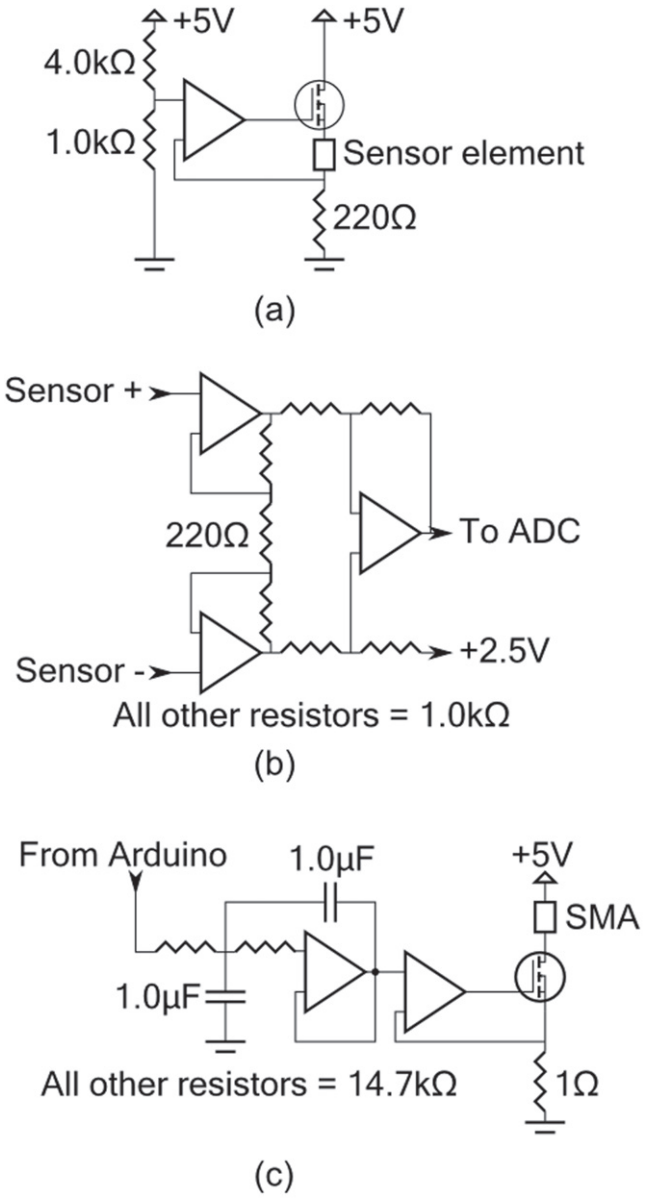

Figure 6. The electronics were fabricated from commercially available components. There were three basic modules: a constant current supply for the strain sensors (a), a differencing amplifier to measure the voltage across the resistive strain sensor (b), and a current supply for the shape memory alloy (c). Modules (a) and (b) are integrated on a custom-built PCB (see figure 1(b)). Module (c) is fabricated on a breadboard.

7. Sensor calibration

The robotic structure used two Dragon Skin 10 Slow strain sensors to determine the the bend angle of the system. In order to accomplish this, the soft structure was held at angles between –60°and 60°at 15° intervals and the sensors were read. Data were collected at each test angle a total of three times in a randomized sequence to eliminate the effects of hysteresis. Generalized least squares regression was used to determine the coefficients for the following equation:

$$\theta = a_0 + a_1 V_1 + a_2 V_2, \quad (1)$$

where θ is the bend angle of the joint, V_1 and V_2 are the voltages across the strain gauges, and a_0, a_1, and a_2 are the coefficients of the fit. Sensor calibration was performed for each elastomer beam. The fit for the non-homogeneous beam is shown in figure 7; it has a 95% confidence interval of 7.53° or 6.28% of the full scale. The fits for the prismatic and non-prismatic beams can be found in figures S1 and S2 (supplemental information). The prismatic beam has a 95% confidence interval of 10.6° or 8.83% of the full scale; the non-prismatic beam has a 95% confidence interval of 5.13° or 4.28% of the full scale.

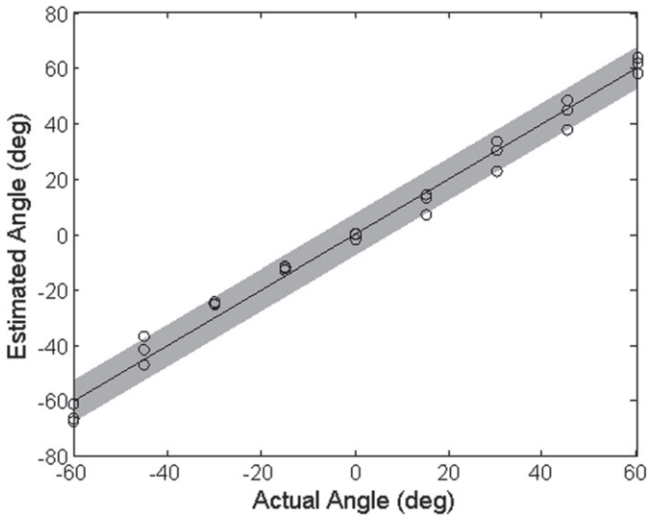

Figure 7. Sensor calibration results for the non-homogeneous beam showing how the actual angle compares to the estimated angle. The shaded region represents the 95% confidence interval.

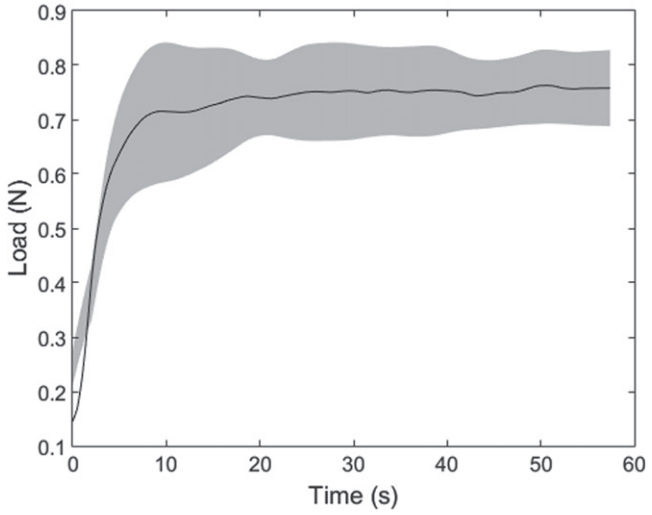

Figure 8. Actuator force generation averaged across three coils with four trials each. Shaded region represents 95% confidence interval. The average data has a symmetric moving average filter across 11 points with uniform weight. The shaded region has a symmetric moving average filter across 41 points with a uniform weight.

8. Actuator performance

Prior to integration into the soft structure, we measured the open-loop performance of the SMA actuator coils. In this test, we used identical coils to those used in the soft structure tests. We fixed the end of the coil in an single-column Instron 3345 materials testing machine, then pulled the coils to simulate the deformation in the actual installation. The initial coil length was 26.2 mm, and the deformed length was 97.0 mm. This latter length matched the nominal length of the coil in a neutral configuration of the soft structure. We then applied a constant current of 0.6 A to heat the wire and cause actuation. We applied current for 60 s, then allowed the actuator to cool for 120 s before repeating the cycle. The resulting blocking force of the actuator was recorded as a function of time and is presented in figure 8. Only the current-on data is shown. The current-off response showed roughly a first-order response, which we expect from free convection. We performed the same test on three coils, cycling the power on and off five times per coil. We discard the data from the first cycle due to start-up transient effects. We believe this is a valid approach since in operation the coils will never be fully cooled or inactive as they were at the start of these tests. The error clouds in figure 8 show the 95% confidence intervals over those four cycles. The 95% confidence interval of the mean values at the end of the test was 0.0764 N, or 10.1% of the average. The non-zero initial value was due to the fact that the actuator does not completely 'turn off' once cooled to room temperature and continues to exhibit purely elastic stress.

9. Controller design optimization

To determine the optimal PID controller design, we tested the system at a number of points in the $\{k_p, k_i, k_d\}$ gain space. We initially explored a larger space on the non-prismatic beam where $k_p \in [2, 20]$, $k_i \in [0, 10]$, and $k_d \in [0, 10]$. From this, we found an optimal solution for all the beams existed in the following subspace: $k_p = \{10, 15, 20\}$, $k_i = \{0.1, 0.4, 0.8\}$, and $k_d = \{0.1, 0.4, 0.8\}$. At each test condition, we drove the system with ten signals, which are a combination of steps and ramps seen in figure S3 (supplemental information). We used these complex signals because we believe they are more representative of actual command histories which might be seen in a soft robotic system, rather than simple step and ramp commands. To evaluate the performance of each controller, we took the sum of the error between the desired and actual angle at 3.3 Hz. The total performance of the controller is the sum of the errors across all ten tests. Once the data were collected, we fit the observations to get an estimated error value of the form given in equation (2) using least-squares regression.

$$E(k_p, k_i, k_d) = A_0 + a_1 k_p^2 + a_2 k_i^2 + a_3 k_d^2 + a_4 k_p k_i + a_5 k_p k_d + a_6 k_i k_d + a_7 k_d + a_8 k_i + a_9 k_d. \quad (2)$$

Figure 9 shows the results matching the actual error to the estimated error for the non-homogeneous beam. The results are all clustered in one area and are relatively close to the 1:1 mapping line shown in black. The inset of figure 9 shows the cluster at the front. It can be seen that we reach a minimum error in the performance of the system. This means that we have reached the noise floor of the system and will not be able to tune it past that floor. Therefore, we take our best solution as the optimal solution, and, thus, selected the optimal from the discrete set rather than finding the optimal on a continuous space. The error clusters for the prismatic and non-prismatic beams are shown in figures S4 and S5 (supplemental information), respectively.

The optimal gains were found to be $k_p = 20$, $k_i = 0.4$, $k_d = 0.1$ for the prismatic beam; $k_p = 15$, $k_i = 0.4$, $k_d = 0.1$

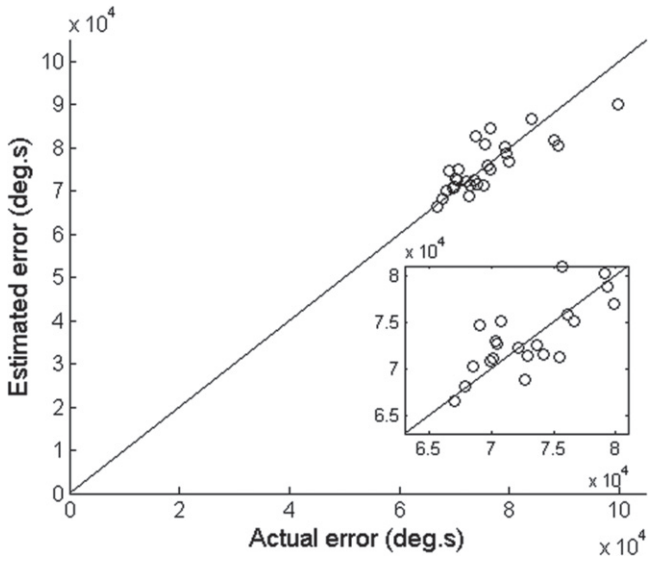

Figure 9. Optimization of PID controller for non-homogeneous beam. Blue dots represent represent test controllers. The line represents the one-to-one mapping of actual sum of errors against the theoretical sum of errors.

for the non-prismatic beam; and $k_p = 20$, $k_i = 0.1$, $k_d = 0.8$ for the non-homogeneous beam. The optimal controller response for the reference signals can be seen in figures S6–S8 (supplemental information) for each of the beams.

10. Results and discussion

To test the effectiveness of our controller, we tested the system with both open- and closed-loop controllers and step and ramp inputs. For the open-loop steps, we sent a pulse width modulated (PWM) signal (30 on a scale of 0–255) from the Arduino to one of the actuators at a time for 90 s. For the open-loop ramps, we sent a growing PWM signal (0–30 on a scale of 0–255) from the Arduino to one of the actuators at a time that grew linearly over 90 s at an update rate of 10 Hz. We then performed the same tests with the optimal controllers we had found previously. Each test was performed three times to look at the repeatability of the system. Figure 10 shows the results of the tests for each of the elastomer beams. The results in blue were driving the arm to 30° in either a step or ramp and the results in red were –30°.

It can be seen for the open-loop step response, the arm settled to a given angle (the same angle over multiple tests), but the response could be slow and the controller did not know the current state of the system. The open-loop ramps for all the beams were significantly worse than the open-loop steps. This was because the SMA has a threshold temperature where it begins actuating and we did not see actuation prior to reaching this temperature. Once it reaches its actuation temperature, it can change quickly, as seen with the open-loop ramps in figure 10(b). These results demonstrated that open-loop control is not sufficient for control of the system.

By closing the loop with our optimal controllers, we drastically changed the response of the system. The settling

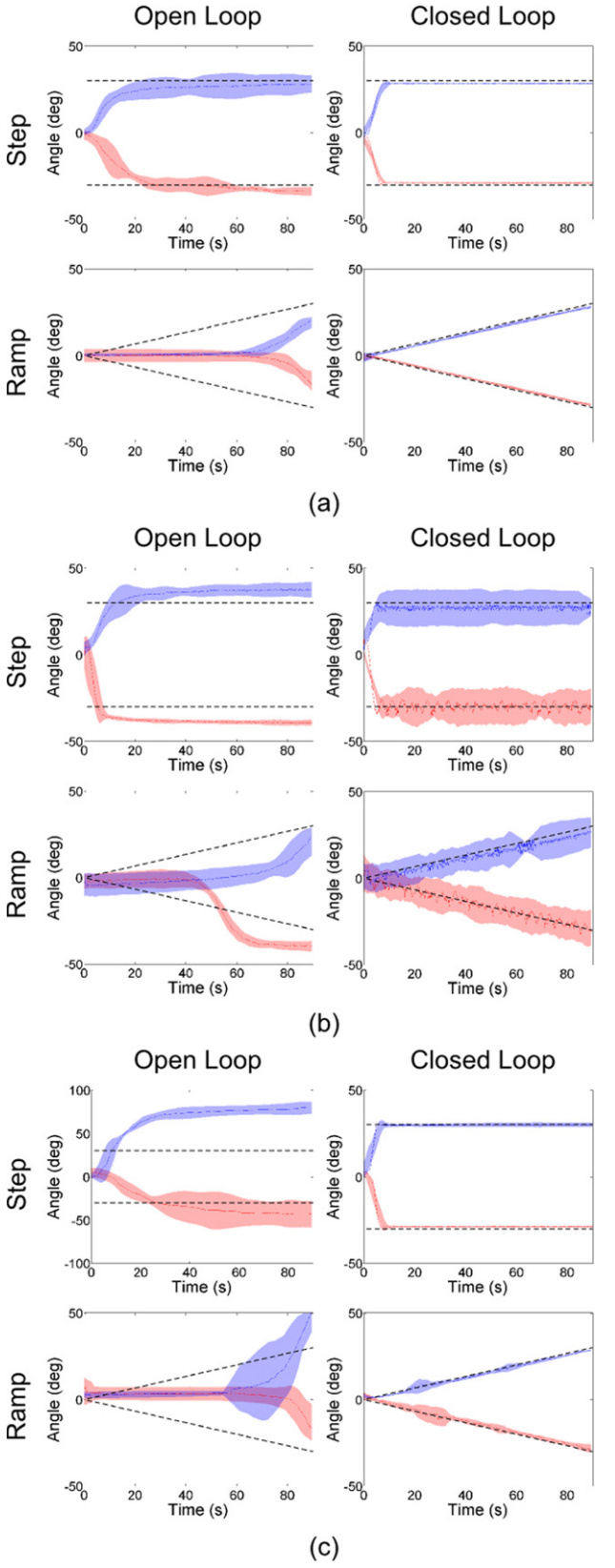

Figure 10. Open-loop and closed-loop results of 30°and –30° steps and ramps for (a) prismatic, (b) non-prismatic, and (c) non-homogeneous beam. Three trials are represented in each graph. The shaded region represents the 95% confidence interval with a moving average filter across 11 points with uniform weight.

time for the open-loop steps ranged from 7.5–42.3 s, while the settling time for the closed-loop steps ranged from 4.5–7.5 s. The closed-loop controllers were able to maintain the desired step and ramp responses considerably better than the open-loop controllers since they did not drift over time like some of the open-loop controllers. The closed-loop ramping responses were able to track the desired ramp.

Looking at the closed-loop response of the different beams, we found that the prismatic beam tracks the steps and ramps very well with little variability in the response. By introducing a joint in the non-prismatic beam, we found that we have greatly altered the response of the system and made it significantly harder to control. We believe this was due to instability in the joint caused by the reduced ratio of bending stiffness to compressive stiffness. Snapping was most pronounced in the non-prismatic beam. The system oscillated around the desired angle rather than being able to maintain position as in the case of a prismatic beam. However, when we reduced the stiffness of the joint, we found that we were able to reobtain a good response. The results from the non-homogeneous beam (recall that this refers to the beam with two dissimilar materials) closely matched the results of the prismatic beam.

The non-homogeneous beam required less power to control than the prismatic beam because it is less stiff and, thus, took less power to move to or maintain a position. This can be seen in figure S8 (supplemental information) where the system did not return to 0° before it started the next test. Another benefit of the non-homogeneous beam was that we have localized the deformation and, thus, know where bending of the beam was taking place. This means we can create jointed soft robotic systems that reduce the degrees of freedom and power consumption in the systems.

11. Conclusion

We have demonstrated closed-loop control of three soft robotic systems. These systems used soft sensors to close the control loop and provide sensory feedback. The degrees-of-freedom of two of the systems were limited by introducing a joint. In one case, the system was left materially homogeneous and, the other, the joint was made from a softer elastomer. This effectively localizes deformations to the joint rather than bending over the length of the whole structure. Reducing the width of the joint, while leaving the beam materially homogeneous made the system harder to control. Furthermore, by making the joint softer, we were able to recover the controllability of the system while reducing power consumption of the system. Soft sensors are beginning to be integrated with soft robots and soft and responsive material actuators, but are not actively being used to control those systems. By integrating control into soft robots, we begin to move towards intelligent, autonomous soft systems.

Acknowledgments

This work was partially supported by an Early Career Faculty grant from NASA's Space Technology Research Grants program (NNX14AO52G). ELW is supported under the National Science Foundation Graduate Research Fellowship program (DGE-1333468). JCC is supported under the NASA Space Technology Research Fellowship program (NNX15AQ75H). Any opinions, findings, and conclusions or recommendations expressed in this material are those of the authors and do not necessarily reflect the views of NASA or the National Science Foundation.

References

[1] Wirtz D C, Schiffers N, Pandorf T, Radermacher K, Weichert D and Forst R 2000 Critical evaluation of known bone material properties to realize anisotropic fe-simulation of the proximal femur *J. Biomech.* **33** 1325–30
[2] Reid K, Young C, Schurr A, Tseng M, Payne R, Keelen P, Miller J and Iyer V 1996 Audiogenic seizures following global ischemia induced by chest compression in long-evans rats *Epilepsy Res.* **23** 195–209
[3] Rus D and Tolley M T 2015 Design, fabrication and control of soft robots *Nature* **521** 467–75
[4] Laschi C and Cianchetti M 2014 Soft robotics: new perspectives for robot bodyware and control *Front Bioeng. Biotechnol.* **2**
[5] Mozeika A, Steltz E and Jaeger H 2009 The first steps of a robot based on jamming skin enabled locomotion *IEEE/RSJ Int. Conf. on Intelligent Robots and Systems IROS 2009* pp 408–9
[6] Steltz E, Mozeika A, Rodenberg N, Brown E and Jaeger H 2009 JSEL: jamming skin enabled locomotion *IEEE/RSJ Int. Conf. on Intelligent Robots and Systems IROS 2009* pp 5672–7
[7] Ilievski F, Mazzeo A D, Shepherd R F, Chen X and Whitesides G M 2011 Soft robotics for chemists *Angew. Chem. Int. Ed.* **50** 1890–5
[8] Shepherd R F, Ilievski F, Choi W, Morin S A, Stokes A A, Mazzeo A D, Chen X, Wang M and Whitesides G M 2011 Multigait soft robot *Proc. Natl Acad. Sci.* **108** 20400–3
[9] Onal C D and Rus D 2013 Autonomous undulatory serpentine locomotion utilizing body dynamics of a fluidic soft robot *Bioinspiration Biomimetics* **8** 026003
[10] Marchese A D and Rus D 2015 Design, kinematics, and control of a soft spatial fluidic elastomer manipulator *Int. J. Robot. Res.* (doi:10.1177/0278364915587925)
[11] Renda F, Cianchetti M, Giorelli M, Arienti A and Laschi C 2012 A 3D steady-state model of a tendon-driven continuum soft manipulator inspired by the octopus arm *Bioinspiration Biomimetics* **7** 025006
[12] Vikas V, Grover P and Trimmer B 2015 Model-free control framework for multi-limb soft robots 2015 *IEEE/RSJ Int. Conf. on Intelligent Robots and Systems (IROS)* pp 1111–6
[13] Farrow N and Correll N 2015 A soft pneumatic actuator that can sense grasp and touch *2015 IEEE/RSJ Int. Conf. on Intelligent Robots and Systems (IROS)* pp 2317–23
[14] Luo M, Pan Y, Skorina E H, Tao W, Chen F, Ozel S and Onal C D 2015 Slithering towards autonomy: a self-contained soft robotic snake platform with integrated curvature sensing *Bioinspiration Biomimetics* **10** 055001
[15] Ogden R W 1997 *Nonlinear Elastic Deformations* (Mineola, NY: Dover)

[16] Findley W N 1989 *Creep and Relaxation of Nonlinear Viscoelastic Materials: With an Introduction to Linear Viscoelasticity* (New York: Dover)

[17] Paik J, Kramer R and Wood R 2011 Stretchable circuits and sensors for robotic origami *2011 IEEE/RSJ Int. Conf. on Intelligent Robots and Systems (IROS)* pp 414–20

[18] Onal C, Wood R and Rus D 2013 An origami-inspired approach to worm robots *IEEE/ASME Trans. Mechatronics* **18** 430–8

[19] Cheng N, Lobovsky M, Keating S, Setapen A, Gero K, Hosoi A and Iagnemma K 2012 Design and analysis of a robust, low-cost, highly articulated manipulator enabled by jamming of granular media *2012 IEEE Int. Conf. on Robotics and Automation (ICRA)* pp 4328–33

[20] Felton S, Tolley M, Onal C, Rus D and Wood R 2013 Robot self-assembly by folding: A printed inchworm robot *2013 IEEE Int. Conf. on Robotics and Automation (ICRA)* pp 277–82

[21] Felton S M, Tolley M T, Shin B, Onal C D, Demaine E D, Rus D and Wood R J 2013 Self-folding with shape memory composites *Soft Matter* **9** 7688

[22] Yu C *et al* 2013 Electronically programmable, reversible shape change in two- and three-dimensional hydrogel structures *Adv. Mater.* **25** 1541–6

[23] Bartlett N W, Tolley M T, Overvelde J T B, Weaver J C, Mosadegh B, Bertoldi K, Whitesides G M and Wood R J 2015 A 3D-printed, functionally graded soft robot powered by combustion *Science* **349** 161–5

[24] Zheng L, Yoshida S, Morimoto Y, Onoe H and Takeuchi S 2015 Pneumatic balloon actuator with tunable bending points *2015 28th IEEE Int. Conf. on Micro Electro Mechanical Systems (MEMS)* pp 18–21

[25] Liu C 2007 Recent developments in polymer MEMS *Adv. Mater.* **19** 3783–90

[26] Rogers J A, Someya T and Huang Y 2010 Materials and mechanics for stretchable electronics *Science* **327** 1603–7

[27] Kramer R, Majidi C, Sahai R and Wood R 2011 Soft curvature sensors for joint angle proprioception *2011 IEEE/RSJ Int. Conf. on Intelligent Robots and Systems (IROS)* pp 1919–26

[28] Filiatrault H L, Carmichael R S, Boutette R A and Carmichael T B 2015 A self-assembled, low-cost, microstructured layer for extremely stretchable gold films *ACS Appl. Mater. Interfaces* **7** 20745–52

[29] Ozel S, Keskin N A, Khea D and Onal C D 2015 A precise embedded curvature sensor module for soft-bodied robots *Sensors Actuators* A **236** 349–56

[30] Case J C, White E L and Kramer R K 2015 Soft material characterization for robotic applications *Soft Robot.* **2** 80–7

[31] Chiechi R C, Weiss E A, Dickey M D and Whitesides G M 2008 Eutectic gallium–indium (EGaIn): a moldable liquid metal for electrical characterization of self-assembled monolayers *Angew. Chem.* **120** 148–50

[32] Dickey M D, Chiechi R C, Larsen R J, Weiss E A, Weitz D A and Whitesides G M 2008 Eutectic gallium–indium (EGaIn): a liquid metal alloy for the formation of stable structures in microchannels at room temperature *Adv. Funct. Mater.* **18** 1097–104

[33] Park Y-L, Majidi C, Kramer R, Brard P and Wood R J 2010 Hyperelastic pressure sensing with a liquid-embedded elastomer *J. Micromech. Microeng.* **20** 125029

[34] Kramer R, Majidi C and Wood R 2011 Wearable tactile keypad with stretchable artificial skin *2011 IEEE Int. Conf. on Robotics and Automation (ICRA)* pp 1103–7

[35] Hammond F, Kramer R, Wan Q, Howe R and Wood R 2012 Soft tactile sensor arrays for micromanipulation *2012 IEEE/RSJ Int. Conf. on Intelligent Robots and Systems (IROS)* pp 25–32

[36] Majidi C, Kramer R and Wood R J 2011 A non-differential elastomer curvature sensor for softer-than-skin electronics *Smart Mater. Struct.* **20** 105017

[37] Park Y-L, Chen B-R and Wood R J 2012 Design and fabrication of soft artificial skin using embedded microchannels and liquid conductors *IEEE Sensors J.* **12** 2711–8

[38] Jackson C, Wagner H and Wasilewski R 1972 55-nitinol-the alloy with a memory: it's physical metallurgy properties, and applications NASA SP-5110 *NASA Special Publication* vol 5110

[39] Liang C and Rogers C A 1992 Design of shape memory alloy actuators *J. Mech. Des.* **114** 223–30

[40] Otsuka K and Ren X 1999 Recent developments in the research of shape memory alloys *Intermetallics* **7** 511–28

[41] Sreekumar M, Nagarajan T, Singaperumal M, Zoppi M and Molfino R 2007 Critical review of current trends in shape memory alloy actuators for intelligent robots *Ind. Robot* **34** 285–94

[42] Bellouard Y 2008 Shape memory alloys for microsystems: a review from a material research perspective *Mater. Sci. Eng.* **481482** 582–9

[43] Lagoudas D C (ed) 2008 *Shape Memory Alloys: Modeling and Engineering Applications* 1st edn (New York: Springer)

[44] Tarnita D, Tarnita D N, Bizdoaca N, Mindrila I and Vasilescu M 2009 Properties and medical applications of shape memory alloys *Romanian Journal of Morphology and Embryology* **50** 15–21

[45] Sun L, Huang W M, Ding Z, Zhao Y, Wang C C, Purnawali H and Tang C 2012 Stimulus-responsive shape memory materials: a review *Mater. Des.* **33** 577–640

[46] Barbarino S, Flores E I S, Ajaj R M, Dayyani I and Friswell M I 2014 A review on shape memory alloys with applications to morphing aircraft *Smart Mater. Struct.* **23** 063001

[47] de Aguiar R A A, de Castro Leão Neto W C, Savi M A and Calas Lopes Pacheco P M 2013 Shape memory alloy helical springs performance: modeling and experimental analysis *Mater. Sci. Forum* **758** 147–56

[48] Seok S, Onal C, Cho K-J, Wood R, Rus D and Kim S 2013 Meshworm: a peristaltic soft robot with antagonistic nickel titanium coil actuators *IEEE/ASME Trans. Mechatronics* **18** 1485–97

[49] Ikuta K, Tsukamoto M and Hirose S 1988 Shape memory alloy servo actuator system with electric resistance feedback and application for active endoscope *Proc. 1988 IEEE Int. Conf. on Robotics and Automation* pp 427–30

[50] Ikuta K 1990 Micro/miniature shape memory alloy actuator *Proc. 1990 IEEE Int. Conf. on Robotics and Automation* pp 2156–61

[51] Ikuta K, Tsukamoto M and Hirose S 1991 Mathematical model and experimental verification of shape memory alloy for designing micro actuator *Proc. IEEE Micro Electro Mechanical Systems. An Investigation of Micro Structures, Sensors, Actuators, Machines and Robots* pp 103–8

[52] Grant D and Hayward V 1997 Variable structure control of shape memory alloy actuators *IEEE Control Syst.* **17** 80–8

[53] Majima S, Kodama K and Hasegawa T 2001 Modeling of shape memory alloy actuator and tracking control system with the model *IEEE Trans. Control Syst. Technol.* **9** 54–9

[54] Gao F, Deng H and Zhang Y 2015 Hybrid actuator combining shape memory alloy with DC motor for prosthetic fingers *Sensors Actuators* A **223** 40–8

[55] Koh J-S and Cho K-J 2009 Omegabot: Biomimetic inchworm robot using SMA coil actuator and smart composite microstructures (SCM) *2009 IEEE Int. Conf. on Robotics and Biomimetics (ROBIO)* pp 1154–9